AIP Journal of Applied Physics

Broad-spectrum light emission at microscopic breakdown sites in metal-insulator-silicon tunnel diodes

J. G. Mihaychuk, M. W. Denhoff, S. P. McAlister, W. R. McKinnon, and A. Chin

Citation: Journal of Applied Physics **98**, 054502 (2005); doi: 10.1063/1.2031946
View online: http://dx.doi.org/10.1063/1.2031946
View Table of Contents: http://scitation.aip.org/content/aip/journal/jap/98/5?ver=pdfcov
Published by the AIP Publishing

Articles you may be interested in
Infrared emission from Ge metal-insulator-semiconductor tunneling diodes
Appl. Phys. Lett. **89**, 261913 (2006); 10.1063/1.2420783

Carrier lifetime measurement on electroluminescent metal–oxide–silicon tunneling diodes
Appl. Phys. Lett. **79**, 2264 (2001); 10.1063/1.1405429

Enhanced reliability of electroluminescence from metal–oxide–silicon tunneling diodes by deuterium incorporation
Appl. Phys. Lett. **78**, 1397 (2001); 10.1063/1.1353817

Hot carrier recombination model of visible electroluminescence from metal–oxide–silicon tunneling diodes
Appl. Phys. Lett. **77**, 4347 (2000); 10.1063/1.1332825

Hot electron impact excitation cross-section of Er 3+ and electroluminescence from erbium-implanted silicon metal-oxide-semiconductor tunnel diodes
Appl. Phys. Lett. **71**, 2824 (1997); 10.1063/1.120147

Re-register for Table of Content Alerts

Create a profile.
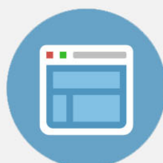
Sign up today!

[This article is copyrighted as indicated in the article. Reuse of AIP content is subject to the terms at: http://scitation.aip.org/termsconditions. Downloaded to] IP: 140.113.38.11 On: Thu, 01 May 2014 02:52:02

Broad-spectrum light emission at microscopic breakdown sites in metal-insulator-silicon tunnel diodes

J. G. Mihaychuk, M. W. Denhoff, S. P. McAlister,[a] and W. R. McKinnon
National Research Council, Institute for Microstructural Sciences, Building M-50, Montreal Road, Ottawa, ON K1A 0R6, Canada

A. Chin
Department of Electronics Engineering, National Chiao Tung University, Hsinchu 300, Taiwan

(Received 14 January 2005; accepted 18 July 2005; published online 6 September 2005)

In addition to Si band-edge electroluminescence (EL) near 1.1 eV, we observe hot-electron EL in metal-insulator-silicon tunnel diodes that can span a detector-limited range from 0.7 to 2.6 eV (1780–480 nm). The maximum photon energy increases with increasing forward bias. In one implementation, sub-micron-sized EL sites appear during the forward-bias stress. The number of sites grows linearly with the current, consistent with the dielectric breakdown of the insulator. We compare the poststress current-voltage data with the quantum-point-contact model. Results are presented for various *p*-type Si(100) devices having 2–8-nm-thick SiO_2, Al_2O_3, and HfO_xN_y insulators. We also describe devices in which electron-beam lithography of an 18-nm-thick SiO_2 is used to define EL sites. © *2005 American Institute of Physics*. [DOI: 10.1063/1.2031946]

I. INTRODUCTION

Silicon is a favored material for photonics as well as microelectronics due to its low cost, established process technology, and high material quality. However, crystalline Si is a very poor light emitter, in which nonradiative recombination exceeds phonon-assisted radiative recombination because the band-gap is indirect. Nevertheless, the work on Si light-emitting devices[1–3] has intensified in the past decade. Increasingly this research addresses eventual performance limitations of integrated circuits.[4,5] A delay in the interconnects will impair signaling across integrated circuits. While optical interconnects might offer a solution,[6] a Si-compatible light source is desirable.

Many electrically driven Si light emitters have used materials such as porous Si,[7] Si-rich oxides,[8,9] Si nanocrystals,[10,11] or rare-earth dopants.[12–15] Another approach[16,17] employed a light-recycling top surface. Recently, stimulated emission was demonstrated[18] in a ridge *pn* diode fabricated using spin-on B dopant and SiO_2 nanoparticles.

Electroluminescence (EL) has also been achieved in planar Si microelectronics using, for example, dislocation loops formed by B implantation[19] or avalanching *pn* junctions.[20–22] EL imaging has been used to analyze Si device operation[23] and reliability.[24,25] Many light emitters have also been implemented as metal-insulator-silicon (MIS) tunnel diodes.[26–37] Recently, Rasras *et al.* outlined the connection between the substrate current and the EL at insulator breakdown sites.[38]

In this work we study MIS devices with SiO_2, Al_2O_3, and HfO_xN_y insulators. We examine visible and infrared EL, including pointlike emission associated with the dielectric breakdown of the insulator. We also demonstrate devices in which conduction and EL occur at locations defined by the electron-beam lithography of a thick SiO_2 layer.

This article is organized as follows. In Sec. II we discuss the mechanisms for both the band-gap and the broad-spectrum EL. Section III outlines a model for postbreakdown current-voltage (*I-V*) characteristics. In Sec. IV we describe the device structures and measurement methods. Section V reports measurement results for several device compositions. We present a detailed discussion of our findings in Sec. VI and more general conclusions in Sec. VII.

II. EL MECHANISMS

A. Band-gap EL

As depicted in Fig. 1 by the transition labeled "1", Si has an indirect band gap with the conduction-band (CB) minimum near the Brillouin zone edge along the Γ-*X* or [100] axis and the valence-band (VB) maxima at the zone center Γ. The radiative recombination of an electron-hole pair requires a third quantum to conserve momentum, normally a phonon. For this reason the nonradiative recombination involving interface states, impurities, and Auger processes dominates. Furthermore, the free-carrier optical absorption in Si can reduce light transmission. Nevertheless, EL in Si occurs with quantum efficiency $\sim 10^{-6}$ and is readily observed using sensitive detectors. The band-gap EL spectra from MIS tunnel diodes have been modeled considering the relevant phonon energies and the contributions of continuum and bound excitons.[35]

B. Broad-spectrum EL

1. Hot-carrier transitions

For MIS devices on *p*-type Si in forward bias, electrons are transported across the insulator to the Si substrate. We therefore consider only the transitions by an electron in a CB, as shown in Fig. 1. However, in addition to CB-VB

[a]Author to whom correspondence should be addressed; electronic mail: sean.mcalister@nrc.ca

[This article is copyrighted as indicated in the article. Reuse of AIP content is subject to the terms at: http://scitation.aip.org/termsconditions. Downloaded to] IP: 140.113.38.11 On: Thu, 01 May 2014 02:52:02

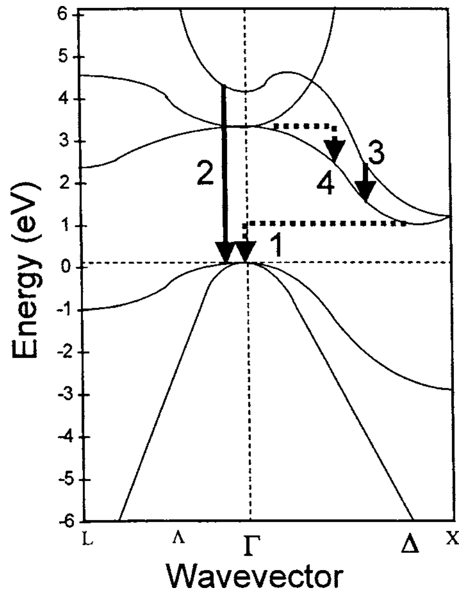

FIG. 1. Si band structure and EL processes. (1) Phonon-assisted ($\Delta k \neq 0$) recombination near the 1.1-eV band gap. (2) Direct ($\Delta k = 0$) recombination of a hot electron. (3) Direct and (4) phonon-assisted hot-electron CB-CB transitions.

transitions (electron-hole recombination), we include CB-CB transitions by energetic electrons. A radiative CB-CB transition may occur in the first CB or between two CB's and can be understood as the inverse process to the free-carrier absorption of photons.

Several workers have modeled[39–41] EL in Si based on transitions of energetic carriers between multiple bands. Both direct and phonon-assisted transitions were considered for CB-VB, CB-CB, and VB-VB cases. The spectra depended strongly on the carrier energy distribution function. Pavesi *et al.* illustrated this for phonon-assisted CB-CB transitions using thermal (Maxwellian) and "box" distributions of injected electrons (see Fig. 8 of Ref. 39). For a thermal distribution with carrier temperature 1700 K, the EL intensity decreased exponentially with increasing photon energy. In contrast a box distribution centered at 4.0 eV with a width of 0.5 eV yielded a slowly varying spectrum from 1.0 to 3.5 eV, with a weaker tail from 3.5 to 4.5 eV and a very abrupt cutoff above 4.5 eV.

Models that use a single steady-state distribution function may be appropriate in some devices. In our devices, however, electrons first enter a hole accumulation layer but may encounter a region of low-field and uniform hole concentrations deeper in the substrate. Thus, electron energy distributions could range from a narrow distribution of tunneling electrons to a thermal distribution in equilibrium with the Si lattice.

Femtosecond-time-resolved photoemission studies[42] in unbiased, atomically clean bulk Si(100) suggest this level of complexity, even in the absence of carrier heating due to an applied electric field. Through electron-electron and electron-phonon scattering electrons rapidly assume a thermal distribution with a temperature much higher than that of the crystal lattice. Through a succession of electron-phonon scattering events, these hot electrons relax to energies near the bottom of the X valley within 1 ps and recombine with holes over much longer time scales. Since both hot and equilibrium electrons may be present simultaneously in MIS tunnel diodes, the EL spectrum will generally include contributions of multiple distribution functions.

2. Above- and below-gap EL

Many studies concerning Si devices address either the visible or the near-IR EL, often due to the spectral range of detectors. We will consider both parts of the spectrum.

Regarding the above-gap EL, several reports address MIS tunnel diodes.[26–34] The model spectra[39] suggest that the above-gap EL results from CB-CB transitions of electrons that have not cooled significantly. The CB-VB transitions can contribute similarly[41] where the hole density is above 10^{19} cm^{-3}. The EL spectrum is expected to shift to shorter wavelengths with increasing forward bias. An alternative proposal[26] stated that the above-gap EL was due to the recombination of hot electrons and holes generated via impact ionization and described by Wolff distributions, given that the observed spectrum did not shift with bias.

Turning to the below-gap EL, one might invoke transitions via defect states within the Si band-gap. However, it is not clear that the spectrum due to defects would span the wide range of photon energies to be considered here. Alternatively, the below-gap EL is compatible with models[39] for the CB-CB EL. Although details depend on the distribution function considered, the intensity of the CB-CB EL between 0.5 and 1 eV can be similar to that of the CB-VB EL.

Finally, we note that the above-gap EL tends to originate in a relatively shallow layer of the Si substrate, while the below-gap EL is free of this restriction. While Si is transparent for photon energies below the band gap, optical absorption becomes increasingly strong as the photon energy increases to above 1.1 eV. For example, while light at 1.55 eV (wavelength $\lambda = 800$ nm) can originate within a depth $\delta = 10\ \mu$m, at 3.10 eV ($\lambda = 400$ nm) one finds that $\delta = 0.1\ \mu$m, where $1/\delta$ is the optical absorption coefficient.[43]

III. CURRENT-VOLTAGE MODEL

In MIS tunnel diodes the physical alteration of the dielectric during a breakdown event should occur preferentially at locations that coincide with thin spots where the electric field is greatest. In addition, the current due to tunneling grows exponentially for a linear decrease in the barrier width. The structure, composition, and electrode-edge effects may also influence the formation of breakdown sites.

In a thorough review of the field, Miranda and Suñé compared[44] several models for the current (or conductance) as a function of voltage following dielectric breakdown in MIS structures with ultrathin insulators. The authors identified several different categories of conduction according to the leakage current level or the current noise/instability: Fowler-Nordheim tunneling, stress-induced leakage current, soft breakdown, hard breakdown, and nonlinear hard breakdown. The quantum-point-contact (QPC) model was found to provide a relatively simple expression for fitting the I-V characteristics following either a soft or a hard breakdown.

[This article is copyrighted as indicated in the article. Reuse of AIP content is subject to the terms at: http://scitation.aip.org/termsconditions. Downloaded to] IP: 140.113.38.11 On: Thu, 01 May 2014 02:52:02

The QPC model serves as a useful reference point for any discussion of postbreakdown *I-V* characteristics in MIS devices.

The QPC model omits direct tunneling and considers nanometer-scale conductive damage channels through a ~5-nm-thick insulator. The lateral confinement leads to the quantization of the transverse momentum for electrons tunneling through these constrictions. The separation between the associated energy subbands is in inverse proportion to the area of the constriction. Conduction occurs by ballistic tunneling transport through a potential barrier of height Φ. In the zero-temperature limit, the total current I through N similar breakdown sites is

$$I = \left(\frac{2e^2}{h}\right) N \left\{ V_c + \frac{1}{\alpha} \ln\left[\frac{1+\exp\{\alpha[\Phi - \beta V_c]\}}{1+\exp\{\alpha[\Phi + (1-\beta)V_c]\}} \right] \right\}, \tag{1}$$

where the potential drop across the constriction is V_c. The quantity α parametrizes the shape of a parabolic potential barrier. The value $0<\beta<1$ represents the fraction of the potential dissipated on the source side of the constriction. The factor $2e^2/h$ is the quantum conductance unit.

The potential drop across the constriction is

$$V_c = V - V_{\text{int}} - IR_{\text{series}}, \tag{2}$$

where V is the externally applied voltage, V_{int} is the internal voltage drop in the semiconductor near the leakage spot and R_{series} is the series resistance. The empirical form of Ref. 45 can be used to represent an increase and saturation of V_{int} with applied voltage:

$$V_{\text{int}} = \left(\frac{2V_0}{\pi}\right) \arctan[(\pi V)/(2V_0)], \tag{3}$$

where V_0 is the limiting value of V_{int} for large values of V. Inclusion of R_{series} means that I appears on the right-hand side of Eq. (1) because of Eq. (2). We evaluate R_{series} as:

$$R_{\text{series}} = r_c + R_{\text{sp}} + R_0, \tag{4}$$

where r_c is the specific contact resistance per unit area for a circular front electrode of radius a, R_{sp} is the substrate spreading resistance, and R_0 is the resistance of the back contact. R_{sp} dominates, and is calculated as follows:[46]

$$R_{\text{sp}} = \rho F/a, \tag{5}$$

$$F = \frac{1}{2\pi} \arctan(2t/a), \tag{6}$$

where ρ and t are the resistivity and thickness of the Si substrate, respectively.

IV. EXPERIMENTAL DETAILS

A. Thin-insulator structure

The devices are depicted in Fig. 2. The thin-insulator devices shown in Fig. 2(a) were fabricated on polished p-type Si(100) wafers with resistivity ρ=5 Ω cm. Some devices were also fabricated on n-type Si to compare the effects of injecting holes rather than of electrons in forward

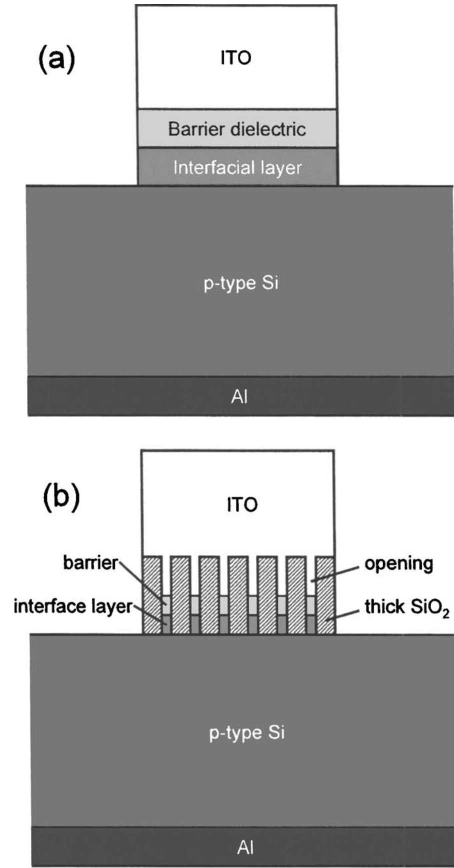

FIG. 2. Device cross sections, not to scale. (a) Thin insulator. (b) Electron-beam-patterned thick oxide.

bias. All wafers were RCA cleaned to remove metallic impurities. The native oxide was then removed using a 5% HF dip. After wafer cleaning, one or more insulating layers were formed. Insulator properties are summarized in Table I and will be discussed in Sec. IV B.

The formation of 100- to 200-nm-thick indium-tin-oxide (ITO) transparent conducting films followed. One method used ac magnetron sputtering of the substrate at 120 °C in O_2/Ar ambient at 3 m Torr. A second method used electron-beam deposition onto a substrate at ambient temperature, followed by annealing for 30 min at 350 °C to oxygenate the film. The films were characterized using transmission electron microscopy (TEM), scanning electron microscopy (SEM), Auger electron spectroscopy (AES), and resistivity measurements. Sputtered films had a columnar polycrystalline structure with ~50-nm grain size, 3.9/40.7/55.4 at. % Sn:In:O content, and resistivity of 6×10^{-4} Ω cm. Electron-beam-deposited films were characterized as having an irregular structure with smaller grains, 22/43.5/54.3 at. % Sn:In:O content, and resistivity of 3×10^{-3} Ω cm. The lower resistivity of the sputtered ITO films is likely due to the higher Sn content.

Contact photolithography and either wet etching or Ar-ion milling defined circular mesas with diameters from 0.1 to 0.6 mm. Al was evaporated to form the back contact to the Si wafer, which was then annealed in forming gas at 400 °C for 10 min.

[This article is copyrighted as indicated in the article. Reuse of AIP content is subject to the terms at: http://scitation.aip.org/termsconditions. Downloaded to] IP: 140.113.38.11 On: Thu, 01 May 2014 02:52:02

TABLE I. Summary of insulator compositions.

	Barrier layer		Interfacial layer		
Device type	Material	Thickness (nm)	Material	Thickness (nm)	Process
TS	SiO_2	2.0	None	0	Thermal oxidation using 400-SCCM[a] O_2 at 500 °C for 15 min.
ET	SiO_2	2.0	SiO_2	2.0	Electron-beam deposition of barrier over thermal SiO_2.
AO	Al_2O_3	2.0	None	0	Evaporating Al and oxidizing in 20-Torr O_2.
AS	Al_2O_3	1.5	SiO_2	1.5	Growing thermal SiO_2, evaporating Al, and oxidizing Al.
sp-AS	Al_2O_3	2.2	SiO_2	2.2	Magnetron sputtering of Al_2O_3 in O_2/ Ar ambient.
HS	HfO_xN_y	4	SiO_2	4	MOCVD of $((C_2H_5)_2N)_4Hf$ and NO.

[a]Standard cubic centimeter per minute.

B. Barrier layers

In Table I, thin-insulator devices are classified according to composition and structure, as determined for uniform films using AES and TEM. The most straightforward structure (denoted as TS) had a front-to-back layer sequence ITO/SiO_2/Si/Al, with thermal SiO_2 grown in a tube furnace. A second structure (denoted as ET) had SiO_2 electron-beam deposited over thermal SiO_2.

Other structures were formed using Al_2O_3. The ITO/Al_2O_3/Si/Al structure with no intentional interfacial layer (denoted as AO) was formed by first evaporating and then oxidizing Al. Structure AS had an additional interfacial thermal SiO_2 layer to form the sequence ITO/Al_2O_3/SiO_2/Si/Al. A variant of AS (sp-AS) used ac magnetron sputtering in 3-mTorr O_2/Ar ambient to form Al_2O_3 over a SiO_2 interfacial layer on a Si wafer at 120 °C. The sp-AS layer structure is shown by the TEM cross section presented in Fig. 3.

The final structure (HS) had the sequence ITO/HfO_xN_y/SiO_2/Si/Al. The barrier and interfacial layers were formed by metal-organic chemical-vapor deposition (MOCVD) using $((C_2H_5)_2N)_4Hf$ and NO. Thicknesses were estimated from capacitance-voltage traces and from TEM of similar samples.

C. Patterned thick-oxide structure

The patterned device structure illustrated in Fig. 2(b) was based on creating openings in an 18-nm-thick layer of thermally grown SiO_2. Following the growth of the SiO_2 layer, electron-beam lithography was used to write square and rectangular features with dimensions as small as 100 nm in polymethylmethacrylate (PMMA) resist. Openings were then wet etched in the SiO_2 to expose the Si substrate. Thin insulating layers were then deposited in the openings. Barrier layers were either thermal SiO_2 or Al_2O_3 formed by oxidation of an evaporated Al film. ITO was electron-beam deposited to fill the openings and form the front contact. Other details were the same as for the thin-insulator devices.

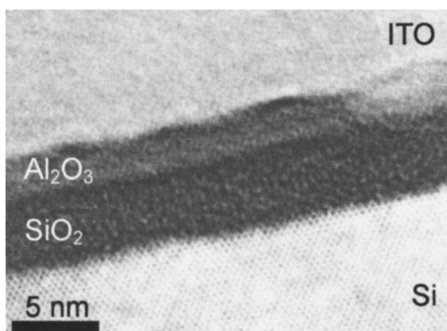

FIG. 3. TEM cross-section of sp-AS sputtered Al_2O_3 With SiO_2 interfacial layer.

D. Measurement techniques

The electrical characterization of the devices involved *I-V* measurements. Devices were placed in a Wentworth low-vibration probe station for data acquisition using an Agilent 4155C semiconductor parameter analyzer. The back was held on a grounded vacuum chuck, and voltage was applied to a tungsten probe placed in contact with the ITO. For the *p*-type Si substrate, forward biasing required a negative potential on the ITO.

Imaging was typically performed using a Nikon Coolpix 990 color charge-coupled device (CCD) camera mounted on a long-working-distance Mitutoyo optical microscope at a low-vibration probe station. The EL from sp-AS devices was also imaged on a cryogenically cooled Jobin-Yvon In GaAs linear array, using narrow-bandpass filters for wavelength selection.

EL spectra were obtained for various devices. To help ensure that the *I-V* and other characteristics of the device did not change during the measurement, devices were subjected to a constant-voltage stress of at least 5 min prior to acquiring each spectrum. The spectra were verified using a number of different systems. Some IR spectra were recorded using Bomem Fourier-transform infrared (FTIR) and CVI 0.25-m grating spectrometers with Ge detectors. Most spectra were acquired by fiber coupling to a Jobin-Yvon Triax-series 180-mm triple-grating spectrometer that used Si and Ge detectors to span the visible and near-IR. Data were corrected for the wavelength dependence of the optics and the detectors.

Spectra were most often acquired from 0.2- or 0.1-mm-diameter circular mesas. A 0.1-mm-diameter-core multimode glass optical fiber was placed near the mesa surface with a small gap for the electrical probe tip. Light coupled through the fiber was transmitted through a gradient-index lens (GRIN) collimator. The collimated light beam was modulated using a Stanford SR540 mechanical chopper and was focused on the spectrometer entrance slit.

[This article is copyrighted as indicated in the article. Reuse of AIP content is subject to the terms at: http://scitation.aip.org/termsconditions. Downloaded to] IP: 140.113.38.11 On: Thu, 01 May 2014 02:52:02

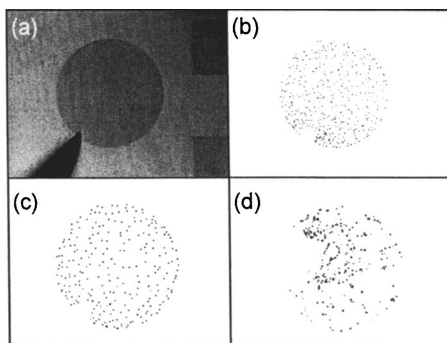

FIG. 4. Micrographs of devices with various barriers and SiO_2 interfacial layer. (a) Illuminated view, unbiased 0.4-mm-diameter ET device (SiO_2 barrier). (b)–(d) Negative EL images for the following forward-biased devices: (b) ET at 9 V and 140 mA; (c) sp-AS (Al_2O_3 barrier), 12.5 V, 81 mA, 0.2-mm diameter; (d) HS (HfO_xN_y barrier), 7 V, 108 mA, 0.1-mm diameter.

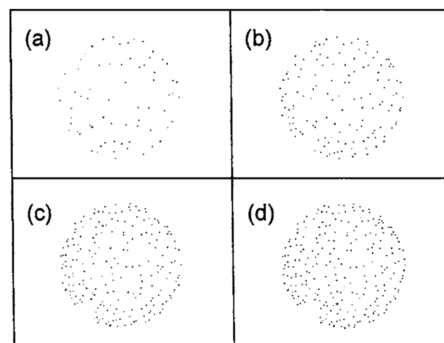

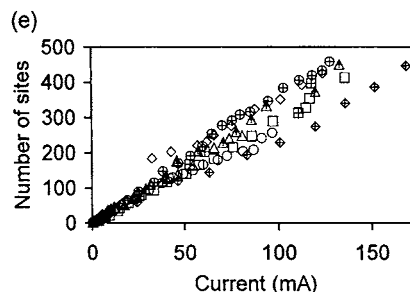

FIG. 5. Number N of EL sites vs forward current I in a virgin device. (a)–(d) Negative images of 0.2-mm-diameter sp-AS device at 22, 47, 66, and 81 mA, respectively. (e) N vs I plot. Open symbols: sp-AS devices. Crossed symbols: ET devices. Each shape denotes mesa diameter in millimeter: (○) 0.1, (△) 0.2, (□) 0.4, and (◇) 0.6.

For wavelengths from 475 to 1000 nm (photon energies 2.61 to 1.24 eV) the detector was a Perkin Elmer (SPCM-series), thermoelectrically cooled, photon-counting Si avalanche photodiode (APD) module with fiber-optic input. The APD output signal was recorded using a Stanford SR400 gated photon counter. For wavelengths in the range from 1000 to 1775 nm (1.24 to 0.70 eV) the detector was a North Coast Scientific EO-series liquid-N_2-cooled high-purity-Ge *p-i-n* photodiode, with electrical signal output via a SR445A preamplifier. Detectors could be reproducibly changed using a fixture at the spectrometer exit port. The detector output was recorded using a SR535 lock-in amplifier interfaced with a computer.

For both sets of detector, diffraction grating, and optics, the slope responsivity of the spectrometer was calibrated at 100-nm intervals and estimated at intermediate wavelengths. The calibration light source used an incandescent lamp and narrow-bandpass filters manufactured by CVI. A 0.15-mm-diameter pinhole aperture was used to emulate the dimensions of an actual device mesa. Within the limitations posed by stray light and higher-order diffraction, the instrument cutoff wavelengths were determined from the spectrum of the unfiltered lamp.

V. RESULTS

A. Thin-insulator devices

In thin-insulator devices visible light emission was seen. As shown in Fig. 4, a pointlike EL was observed in forward bias in several devices having different barriers and interfacial layers. With reference to Table I, the compositions represented in Fig. 4 are evaporated and thermal SiO_2 (ET), sputtered Al_2O_3/SiO_2 (sp-AS) and MOCVD HfO_xN_y/SiO_2 (HS). While the specific examples shown were obtained in constant-voltage mode, similar results may also be obtained by applying a constant-current stress.

Multiple light-emitting sites appeared during the first application of constant forward-bias voltage to the device. The current was monitored throughout, and we found that more sites appeared at higher biases. Once a given upper limit of bias was reached, the number of EL sites remained roughly constant if the voltage was varied but kept below this upper limit. During such a variation of biases, the total EL intensity was proportional to the current. A small fraction of sites (less than 1%) may either appear as new sites or cease to emit light, but the majority of the sites are stable. Most sites simply became brighter or dimmer as the current increased or decreased, respectively. Viewed through the microscope at 500× magnification, individual sites appeared as points; i.e., their size was significantly smaller than 1 μm. Devices seen through the microscope also appeared to have dim, nearly uniform, light emission over the entire mesa that was below the noise floor in high-magnification micrographs.

The EL color varied from site to site. In a color image corresponding to Fig. 4(c), for example, the apparent color ranges from red to orange to yellow. This suggests that the properties of each site vary. EL sites were also imaged using an InGaAs linear array and were found to emit below (e.g., at 1400 nm), near (at 1100 nm), and above (e.g., at 900 nm) the band gap. At 1100 nm, EL was present both at pointlike sites and in a more uniform distribution across the entire mesa. At other wavelengths EL was measured only at the pointlike sites.

Figure 5 shows the increase of the number N of EL sites as the current I in a forward-biased virgin device increased. The images in Figs. 5(a)–5(d) show a 0.2-mm-diameter sp-AS device subjected to progressive increases in forward bias in a constant-voltage mode. Where the number of EL sites exceeded ten, it was determined automatically using IMAGEPRO machine-vision software. Manual and automated counts were verified as equivalent for up to 50 sites.

In Fig. 5(e) we plot the linear increase of N with I for several virgin devices during the first application of forward bias. Two structures are represented, both with SiO_2 interfa-

[This article is copyrighted as indicated in the article. Reuse of AIP content is subject to the terms at: http://scitation.aip.org/termsconditions. Downloaded to] IP: 140.113.38.11 On: Thu, 01 May 2014 02:52:02

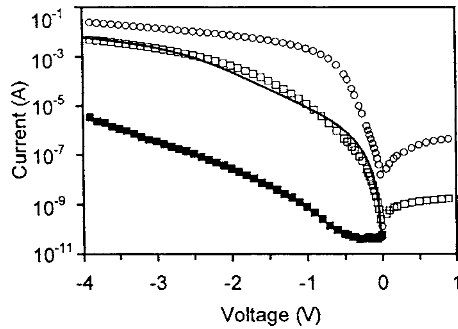

FIG. 6. *I-V* curves. Top: TS device (○). Middle: data from sp-AS device after stress (□), with fit to QPC model (bold line). Bottom: virgin sp-AS device (■).

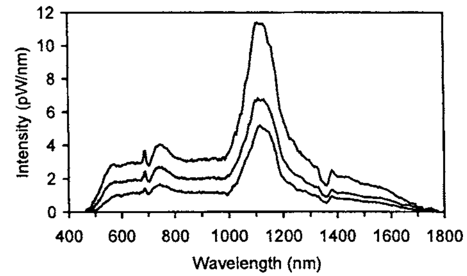

FIG. 7. Spectra from 0.1-mm-diameter ET device at the following forward-bias levels: 11 V and 72 mA (top); 9 V and 49 mA (middle); 7 V and 30 mA (bottom). Features near 700 and 1350 nm are artifacts of the coarse calibration.

cial layers: sp-AS (Al_2O_3 barrier) and ET (SiO_2 barrier). The observed behavior was similar regardless of the composition of the insulator layers or the device area. The slope indicates an average current increase of 0.3 mA per light-emitting site. The linear increase suggests that each EL site acted as an antifuse formed by dielectric breakdown. If we assume that the diameter of a breakdown spot was from 100 to 10 nm, the local current density was from 10^6 to 10^8 A/cm^2, respectively.

In Fig. 6 we show experimental *I-V* data for both "virgin" devices and stressed devices. We compared the *I-V* characteristics with the mechanisms presented by Miranda and Suñé.[44] The virgin *I-V* curve for the sp-AS device (Al_2O_3 barrier) is consistent with either stress-induced leakage current for small N or soft breakdown for larger N. Direct tunneling is expected to make a lesser contribution to the current due to the relatively thick (4.4 nm) barrier and interfacial layers. While no light emission was observed by eye for the virgin sp-AS device, this may simply have been due to the relatively low current.

The current in a sp-AS device following constant-voltage stress for 5 min at 10 V and 100 mA was several orders of magnitude greater than that in the virgin device. A large number of pointlike sites for the visible EL were observed in forward bias. The magnitude of current present in the poststress sp-AS *I-V* curve was similar to the hard breakdown examples in Ref. 44. On the other hand, one cannot exclude the soft breakdown occurring at a large number N of sites.

The QPC model has the advantage of being equally applicable to both soft and hard breakdown modes. The heavy line plotted in Fig. 6 is a fit of Eq. (1) to the forward-bias poststress sp-AS *I-V* curve, with the number of sites and the series resistance as input parameters. We found $N \approx 200$ from a count of EL sites in an image of the device operated at maximum stress. In addition, we found $R_{\text{series}} \approx 140\ \Omega$ for a 0.2-mm-diameter mesa from the slope at a high bias of the *I-V* curve of an Al–Si Schottky diode that was fabricated on a comparable substrate. The parameters obtained from the fit were $\Phi = 1.26$ V, $V_0 \approx 1.53$ V, $\alpha = 5.12$ V^{-1}, and $\beta = 0.89$. Given the observed color diversity, we emphasize that each site was distinct, so that these parameters are average values. Nevertheless, this particular *I-V* curve and the values of the parameters obtained from the fit are representative of many measurements on several sp-AS devices. Qualitatively similar *I-V* curves can be obtained for other devices that exhibit a pointlike light emission, although the exact fit parameters vary primarily with the insulator thickness and secondarily with the insulator composition. The greatest deviation of the fit from the measured data occurs between about 0.5 and 2.0 V, marking the transition to the series-resistance-limited conduction at high biases.

The top curve in Fig. 6 represents a TS device with a single 2-nm thermal SiO_2 layer. Only a few breakdown events were observed at relatively high biases. Below 4.5 V, the *I-V* curves for stressed TS devices generally reproduced the virgin curves. The TS device *I-V* followed the diode equation with ideality factor $n = 2.1$ up to 0.5 V. A forward-bias operation was accompanied by a dim visible EL that was relatively uniform across the entire mesa, without any pointlike sites. It appears that tunneling through the thin barrier was favored over the formation of luminescent breakdown sites.

For ET, AO, AS, sp-AS, and HS devices, the Si band-gap peak near 1100 nm was bracketed by emission in a broad range of shorter and longer wavelengths. As an example, the spectra for different forward-bias voltages are presented in Fig. 7 for an ET device. We emphasize that devices were subjected to constant-voltage electrical stress prior to the acquisition of EL spectra, so that *I-V* and other characteristics do not change significantly during the course of the measurement. The light intensity varied linearly with current. The external quantum efficiency for the above-gap EL measured for an sp-AS device was about 10^{-7}, in line with expectations for band-gap Si light emitters. With respect to the power conversion efficiency, using a pW-precision meter, we found that for a 10-V bias and a 100-mA current (1 W electrical power dissipation) the external optical power detected was 10 nW each in the above-gap (Si photodiode) and below-gap (Ge photodiode) wavelength ranges. Much of the electrical power dissipation was due to the series resistance of the substrate.

Figure 8 shows the spectrum from a TS device at a forward bias of 5 V and a current of 85 mA. Given that the insulator was thinner than in the sp-AS case, the current for a given voltage was higher (see Fig. 6), consistent with direct tunneling. No pointlike visible EL was evident. Relative to sp-AS and ET devices, the band-gap EL was strong and the above-gap EL was weak. No below-gap EL was measured at wavelengths longer than about 1300 nm.

[This article is copyrighted as indicated in the article. Reuse of AIP content is subject to the terms at: http://scitation.aip.org/termsconditions. Downloaded to] IP: 140.113.38.11 On: Thu, 01 May 2014 02:52:02

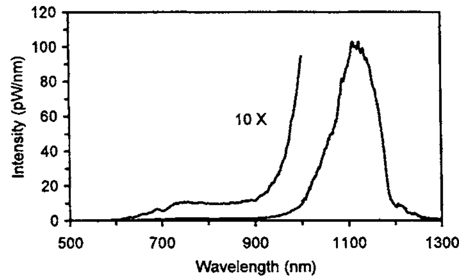

FIG. 8. Spectrum from TS device at forward bias of 5 V and 85 mA. Above-gap EL is shown multiplied ten times for clarity.

Some sp-AS devices were also made on n-type Si. No pointlike sites for EL were evident, although dielectric breakdown features were still present in the I-V curve. For the forward-biased n-type device (ITO at positive potential) only the band-gap peak was observed. We therefore emphasize that the broad-spectrum EL was associated primarily with electron injection into p-type Si.

As Fig. 7 shows for the ET device, the spectrum shifted to shorter wavelengths as the forward bias was increased. The shift is consistent with an increase in the energy of electrons in the Si CB. By linearly extrapolating the short-wavelength tail to zero intensity, as in Fig. 9(a), we were able to estimate the maximum photon energy present. The maximum photon energy, plotted as a function of the forward-bias voltage in Fig. 9(b), increased monotonically with the bias for ET, sp-AS, and TS devices. Although the increase in the cutoff photon energy was rapid at low biases, the effect began to saturate by 5 V, where series resistance dominates. An earlier study[26] found that the visible spectrum from ITO/SiO_2/Si tunnel diodes was insensitive to biases from about 6 to 9 V; however, the authors did not report results for lower voltages.

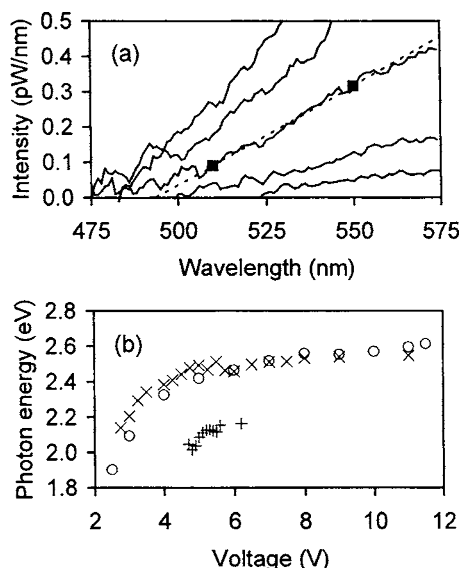

FIG. 9. Shift of spectrum with increasing forward bias. (a) Short-wavelength EL for sp-AS device from 9 V (top) to 5 V (bottom) in 1 V steps. Dashed line, squares: example linear fit to tail at a 7 V bias. (b) Maximum photon energy vs bias: (×) sp-AS, (○) ET, (+) TS.

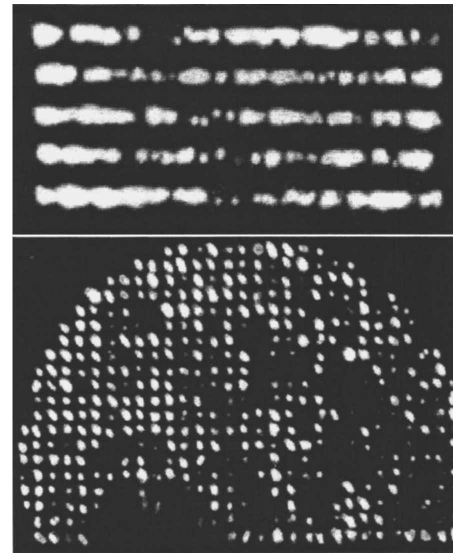

FIG. 10. Micrographs of electron-beam-patterned AO devices operated in forward bias. Top: five 1-μm-wide lines, at 11 V and 45 mA. Bottom: array of 1-μm squares, at 15 V and 100 mA, with lower left obscured by the electrical probe tip.

B. Patterned thick-oxide devices

Optical micrographs of patterned devices operated in forward bias, such as those shown in Fig. 10, showed visible EL only in the openings defined using electron-beam lithography. The color and brightness varied from one location to another in a manner similar to the thin-insulator devices. For the square-array device operated at a 15-V bias and a 100-mA current depicted in Fig. 10, about 400 of the 519 square windows emitted light. In comparison, thin-insulator devices had about 300 pointlike EL sites at the same current. The spectra were similar in form for both patterned and unpatterned devices. Changing the barrier from Al_2O_3 to thermal SiO_2 did not significantly alter the behavior.

I-V curves for patterned devices were similar to those for unpatterned devices. For devices with the same number of square windows, the I-V characteristics were independent of the size of the windows, for sizes of 1 μm, 500, 300, or 100 nm. The current at a given voltage varied little despite a hundredfold change in the window area. The similarity of current levels, number of EL sites, and spectra suggests that current flow may have been via breakdown sites in both patterned and unpatterned devices. If so, then each square must typically have contained one site with dimensions less than the smallest window size of 100 nm.

In layer structures where unpatterned devices showed pointlike visible EL, patterned devices also showed pointlike EL. Since negligible current was expected to flow through the 18-nm-thick oxide, and the current levels were similar, it is likely that almost all current passed through the light-emitting regions in both cases. As another example of the importance of current concentration in visible EL, patterned devices with a thermal SiO_2 insulator produced visible EL whereas unpatterned TS devices produced little above-gap EL (Fig. 8). Thus visible EL was associated with current concentration, whether at a breakdown site or at a window in a thick SiO_2.

[This article is copyrighted as indicated in the article. Reuse of AIP content is subject to the terms at: http://scitation.aip.org/termsconditions. Downloaded to] IP: 140.113.38.11 On: Thu, 01 May 2014 02:52:02

VI. DISCUSSION

We observed broad-spectrum EL from several MIS tunnel diodes. We found pointlike EL sites in devices with a variety of insulators. The number of sites increased in proportion to the forward current, suggesting the formation of breakdown sites. The observations were independent of the growth method used to form the ITO.

It is interesting to compare the spectra associated with pointlike EL (e.g., ET or sp-AS) with devices with more spatially uniform EL (TS). In ET and sp-AS devices, the broad-spectrum EL was enhanced, and the band-gap peak was relatively weak. The converse was true for TS devices. Relative to the ET device operated at 72 mA (see Fig. 7), the TS device at 85 mA (see Fig. 8) exhibited a ten-fold greater band-gap EL, but a 4.5-times lower integrated EL at wavelengths less than 900 nm. The measured photon energy ranges at a 5-V bias were 1.0–2.1 eV for the TS device, compared with 0.7–2.4 eV for the ET device.

The variation in the band-gap and broad-spectrum components leads one to consider the origins of each. Regarding the band-gap EL, an electron tunneling into Si can relax to a state near the CB minimum through multiple electron-phonon scattering events. While a nonradiative recombination with a hole usually follows, a phonon-assisted radiative recombination can sometimes occur. The resulting peak has photon energies slightly below the Si band-gap.

EL at photon energies far from the band-gap is consistent with hot-electron radiative transitions in Si. For a sufficiently energetic distribution of tunneling electrons, CB-CB or CB-VB EL can span a large range of visible and near-IR photon energies.[39] In devices on *n*-type Si we observed only the band-edge EL, which suggests that hot-hole VB-VB processes are not effective.

Si metal-oxide-semiconductor field-effect transistor (MOSFET) models[39–41] predict slowly varying CB-CB EL from 0.5 to 1.0 eV (2480 to 1240 nm), similar to what we observed (Fig. 7.) A model of our devices should account for tunneling, scattering, drift, and diffusion in the vicinity of a breakdown site with submicron lateral extent. A constraint would be that electrons cool over a distance of not more than several hundred nanometers, based on the apparent size of the visible EL sites.

In devices with a pointlike EL, the enhanced broad-spectrum EL was accompanied by the relatively weak band-gap EL. However, it is not clear if the hot-electron EL would alter the subsequent radiative recombination involving electrons near the CB minimum. Instead, the diminished band-gap EL may be associated with the enhanced nonradiative recombination due to an increase in the density of interface states near a breakdown site. While other workers[28] have suggested a direct competition between the visible and the band-edge EL, this appears unlikely. Given the low quantum efficiency, the hot-carrier EL only involves a negligible fraction of the total number of carriers available to participate in the band-gap EL.

The bias dependence of the high-photon-energy cutoff suggests that the distribution function for electrons in the Si CB undergoes a corresponding shift to higher energies. We found that the spectrum shifted substantially at a low bias, where the voltage drop due to series resistance is small. It appears that Liu *et al.* did not observe a similar effect[26] because their results were obtained at a relatively high bias, where the effect saturates. The apparent lack of sensitivity to bias led Liu *et al.* to propose a mechanism for the visible EL involving the recombination of hot electrons and hot holes after the impact ionization. However, impact ionization would produce a quadratic variation of light intensity with current,[47] whereas we measured a linear variation.

We also note that our results differed from the models of Asli *et al.*,[48] who predicted that the above- and below-gap EL should be three to five orders of magnitude below the band-gap peak. We found that these features were often comparable in intensity.

VII. CONCLUSIONS

Using MIS tunnel diodes with ITO transparent electrodes, we have explicitly identified and studied EL at submicron-sized breakdown sites. Our devices can support hundreds of pointlike breakdown sites without a catastrophic failure of the device.

We have also used electron-beam lithography to pattern sites for conduction and EL in thick-oxide devices. By studying a variety of structures at both visible and near-IR wavelengths, we have gained a more complete understanding of the EL phenomena.

In particular we have shown that the band-gap peak can be bracketed at lower and higher photon energies by broad features of similar intensity. For devices where current flow and EL are associated with breakdown sites, the broad-spectrum EL was enhanced and the band-gap EL was diminished, relative to devices with a thin thermal SiO_2 barrier. The spectra were consistent with a combination of the hot-electron radiative transitions and the band-gap recombination.

An important application of light-emission microscopy concerns visualization of leakage current. Scaled MOSFET's require thicker, low-leakage gate dielectrics. To achieve the desired transconductance high-κ materials are introduced to maintain the capacitance. EL imaging and spectroscopy can be used to study leakage and breakdown in these materials.

Despite the low external quantum efficiency ($\sim 10^{-7}$) of EL, the small size of the pointlike EL sites may prove useful. Furthermore, the number of sites created for a given current is independent of mesa size, in the range of sizes studied. On this basis it should be possible to make smaller light-emitting devices on Si, using a low-resistivity substrate and/or a shallow active region to reduce the spreading resistance.

ACKNOWLEDGMENTS

This work was carried out under the NRC-NSCT collaboration on "RF & Optical Wireless Interconnects for VLSI IC." We gratefully acknowledge technical assistance from H.T. Tran, P. Ma, J. Lapointe, M. Lee, D. Landheer, X. Wu, J.W. Fraser, S. Moisa, M. Beaulieu, J.M. Fraser, S. Raymond, and N. Rowell.

[This article is copyrighted as indicated in the article. Reuse of AIP content is subject to the terms at: http://scitation.aip.org/termsconditions. Downloaded to] IP: 140.113.38.11 On: Thu, 01 May 2014 02:52:02

[1]D. A. B. Miller, Nature (London) **384**, 307 (1996).
[2]S. S. Iyer and Y.-H. Xie, Science **260**, 40 (1993).
[3]L. Pavesi, J. Phys.: Condens. Matter **15**, R1169 (2003).
[4]See, for example, *Silicon Photonics*, Topics in Applied Physics Vol. 94, edited by L. Pavesi and D. J. Lockwood (Springer, Berlin, 2004); Physica E (Amsterdam) **16** (2003); and Intel Technol. J. **8**, No. 2 (2004) (http://developer.intel.com/technology/ITJ/)
[5]D. A. B. Miller, IEEE J. Sel. Top. Quantum Electron. **6**, 1312 (2000).
[6]International Technology Roadmap for Semiconductors, http://public.itrs.net/
[7]S. Lazarouk, P. Jaguiro, S. Katsouba, G. Masini, S. La Monica, G. Maiello, and A. Ferrari, Appl. Phys. Lett. **68**, 1646 (1996).
[8]K. D. Hirschman, L. Tsybeskov, S. P. Duttagupta, and P. M. Fauchet, Nature (London) **384**, 338 (1996).
[9]L. Tsybeskov, S. P. Duttagupta, K. D. Hirschman, D. G. Hall, and P. M. Fauchet, Appl. Phys. Lett. **69**, 3411 (1996).
[10]J. De La Torre *et al.*, Physica E (Amsterdam) **16**, 326 (2003).
[11]A. Irrera *et al.*, Physica E (Amsterdam) **16**, 395 (2003).
[12]A. Polman, J. Appl. Phys. **82**, 1 (1997).
[13]M. E. Castagna *et al.*, Physica E (Amsterdam) **16**, 547 (2003); M. E. Castagna *et al.*, Mater. Sci. Eng., B **105**, 83 (2003).
[14]Ch. Buchal *et al.*, Nucl. Instrum. Methods Phys. Res. B **190**, 40 (2002).
[15]Ch. Buchal, S. Wang, F. Lu, R. Carius, and S. Coffa, Nucl. Instrum. Methods Phys. Res. B **190**, 40 (2002).
[16]M. A. Green, J. Zhao, A. Wang, P. J. Reece, and M. Gal, Nature (London) **412**, 805 (2001).
[17]J. Zhao, M. A. Green, and A. Wang, J. Appl. Phys. **92**, 2977 (2002).
[18]M. J. Chen, J. L. Yen, J. Y. Li, J. F. Chang, S. C. Tsai, and C. S. Tsai, Appl. Phys. Lett. **84**, 2163 (2004).
[19]W. L. Ng, M. A. Lourenco, R. M. Gwilliam, S. Ledain, G. Shao, and K. P. Homewood, Nature (London) **410**, 192 (2001).
[20]M. du Plessis, H. Aharoni, and L. W. Snyman, IEEE J. Sel. Top. Quantum Electron. **8**, 1412 (2002).
[21]M. Lahbabi *et al.*, Appl. Phys. Lett. **77**, 3182 (2000).
[22]A. T. Obeidat, Z. Kalayjian, A. G. Andreou, and J. B. Khurgin, Appl. Phys. Lett. **70**, 470 (1997).
[23]J. C. Tsang, J. A. Kash, and D. P. Vallet, Proc. IEEE **88**, 1440 (2000).
[24]C. Leroux and D. Blachier, Microelectron. Eng. **49**, 169 (1999).
[25]A. Chatterjee and B. Bhuva, IEEE Trans. Device Mater. Reliab. **2**, 60 (2002).
[26]C. W. Liu, S. T. Chang, M. J. Chen, and C. F. Lin, Appl. Phys. Lett. **77**, 4347 (2000).
[27]A. Chin, C. S. Liang, C. Y. Lin, C. C. Wu, and J. Liu, *IEDM Technical Digest*, International Electron Devices Meeting, 2001, Washington, D. C., 2–5 December 2001 (IEEE, Piscataway, NJ, 2001), p. 171.
[28]E. Cartier, J. C. Tsang, M. V. Fischetti, and D. A. Buchanan, Microelectron. Eng. **36**, 103 (1997).
[29]M. J. Chen, C. F. Lin, W. T. Liu, S. T. Chang, and C. W. Liu, J. Appl. Phys. **89**, 323 (2001).
[30]Y. Q. Wang, T. P. Zhao, J. Liu, and G. G. Qin, Appl. Phys. Lett. **74**, 3815 (1999).
[31]C. Y. Lin, A. Chin, Y. T. Hou, M. F. Li, S. P. McAlister, and D. L. Kwong, IEEE Photon. Technol. Lett. **16**, 36 (2004).
[32]R. Versari, A. Pieracci, M. Manfredi, G. Soncini, P. Bellutti, and B. Ricco, *IEDM Technical Digest*, International Electron Devices Meeting, 1999, Washington, D.C., 5–8 December 1999 (IEEE, Piscataway, NJ, 1999), p. 745.
[33]L. Heikillä, T. Kuusela, and H.-P. Hedman, J. Appl. Phys. **89**, 2179 (2001).
[34]N. Porjo, T. Kuusela, and L. Heikillä, J. Appl. Phys. **89**, 4902 (2001).
[35]M. J. Chen, J. F. Chang, J. L. Yen, C. S. Tsai, E. Z. Liang, C. F. Lin, and C. W. Liu, J. Appl. Phys. **93**, 4253 (2003).
[36]M. J. Chen, E. Z. Liang, S. W. Chang, and C. F. Lin, J. Appl. Phys. **90**, 789 (2001).
[37]C. W. Liu, M. H. Lee, M. J. Chen, I. C. Lin, and C. F. Lin, Appl. Phys. Lett. **76**, 1516 (2000).
[38]M. Rasras, I. De Wolf, G. Groeseneken, R. Degraeve, and H. E. Maes, J. Appl. Phys. **91**, 2155 (2002).
[39]M. Pavesi, P. L. Rigolli, M. Manfredi, P. Palestri, and L. Selmi, Phys. Rev. B **65**, 195209 (2002).
[40]S. Villa, A. L. Lacaita, and A. Pacelli, Phys. Rev. B **52**, 10993 (1995).
[41]J. Bude, N. Sano, and A. Yoshii, Phys. Rev. B **45**, 5848 (1993).
[42]J. R. Goldman and J. A. Prybyla, Phys. Rev. Lett. **72**, 1364 (1994).
[43]D. F. Edwards, in *Handbook of Optical Constants of Solids*, edited by E. D. Palik (Academic, Orlando, 1985), pp. 547–569.
[44]E. Miranda and J. Suñé, Microelectron. Reliab. **44**, 1 (2004).
[45]E. Miranda and J. Suñé, Microelectron. Reliab. **40**, 1599 (2000).
[46]D. K. Schroder, *Semiconductor Material and Device Characterization*, 2nd ed. (Wiley, New York, 1998), Chap. 3.4, p. 143.
[47]G. Deboy and J. Kölzer, Semicond. Sci. Technol. **9**, 1017 (1993).
[48]N. Asli, A. F. Shulekin, P. D. Yoder, M. I. Vexler, I. V. Grekhov, and P. Seegebrecht, Solid-State Electron. **48**, 731 (2004).

[This article is copyrighted as indicated in the article. Reuse of AIP content is subject to the terms at: http://scitation.aip.org/termsconditions. Downloaded to] IP: 140.113.38.11 On: Thu, 01 May 2014 02:52:02